


## Article

# Life Cycle Assessment of Various PMSG-Based Drivetrain Concepts for 15 MW Offshore Wind Turbines Applications

Farid Khazaeli Moghadam \* and Nils Desch 

Department of Marine Technology, Norwegian University of Science and Technology, 7491 Trondheim, Norway

\* Correspondence: farid.k.moghadam@ntnu.no

**Abstract:** There are different configurations selected by both industry and academia as the drivetrain for wind turbines in the power range of 10 to 16 MW. The choice of drivetrain system influences the levelized cost of energy, and, as the turbines become larger, and, therefore, costlier, there is more potential for the optimization of cost critical systems, like the drivetrain. The latter motivates the utilization of a life cycle assessment approach to profoundly influence the choice of drivetrain technology such that it offers a better compromise between the different aspects in the drivetrain life cycle. To this end, in this paper, various permanent magnet synchronous generator (PMSG)-based drivetrain technologies for 15 MW bottom-fixed and floating offshore wind turbine applications are designed and compared. The technologies under investigation are based on direct-drive, medium- and high-speed generators. The conceptual design of the drivetrain for the three technologies under consideration is investigated and the pros and cons of each technology are assessed and explained by looking, simultaneously, into the design, manufacturing, operation and maintenance.

**Keywords:** drivetrain; dynamic analysis; gearbox; life cycle assessment; offshore wind turbine; optimization; permanent magnet synchronous generator.



**Citation:** Moghadam, F.K.; Desch, N. Life Cycle Assessment of Various PMSG-Based Drivetrain Concepts for 15 MW Offshore Wind Turbines Applications. *Energies* **2023**, *16*, 1499. <https://doi.org/10.3390/en16031499>

Academic Editor: Taimoor Asim

Received: 4 January 2023

Revised: 23 January 2023

Accepted: 28 January 2023

Published: 2 February 2023



**Copyright:** © 2023 by the authors. Licensee MDPI, Basel, Switzerland. This article is an open access article distributed under the terms and conditions of the Creative Commons Attribution (CC BY) license (<https://creativecommons.org/licenses/by/4.0/>).

## 1. Introduction

The installed capacity of offshore wind power in Europe increased from about 3 GW in 2009 to about 22 GW in 2019, and is growing even faster in attempts to realize the European Union (EU) climate-neutralization goal by 2050. To reach this goal, renewable energy has to increase from 32% to 40% by 2030, which demands 451 GW of wind power capacity by 2030. To reach this capacity, 271 GW new installations [1] are called for. The United States is also planning to increase its installed offshore wind power from 30 MW in 2020 to as much as 30 GW by 2030 [2]. Offshore wind is an enabler for the utilization of larger turbines. The rated power of wind turbines is increasing with a fast pace. Increasing the size of offshore wind turbines is an effective measure to lower the levelized cost of energy (LCOE) [3]. The largest commercially available turbine is currently 16 MW [4]. The largest available reference research turbine is 20 MW [5]. Research has been carried out on the different aspects of design and analysis of turbines with a rated power up to 50 MW [6,7], which is much higher than what is currently available in industry, showing that wind turbines of higher-rated power are expected in the wind power market in the upcoming future.

The power train system, consisting of back-to-back (BTB) frequency converter, generator, gearbox, shafts, main bearings and rotor assembly, is responsible for 46% of the LCOE of land-based wind turbines [8]. This contribution is expected to be lower in offshore applications, due to a lower contribution of turbine components and O&M in the LCOE [8]. The high contribution of the power train system in the LCOE motivates the employment of the life cycle assessment approach in a bid to reduce the overall costs. In the power train system, the drivetrain converts the variable input mechanical power to regulated electrical power at the desired voltage and frequency, and transmits the non-torque loads to the bed-plate and tower. The drivetrain in our definition includes the entire power

conversion system from the main bearings to the electrical generator and power-frequency converter system. The two main drivetrain technologies, namely direct-drive and geared drivetrain systems, and the components that characterize them are depicted in Figure 1. Beside the rotor–gearbox–generator configuration, there are other alternatives, such as hydraulic transmission systems, to realize the wind turbine drivetrain [9], which are not discussed in this work.

Today's largest commercially available wind turbine drivetrain systems are MHI Vestas 15 MW, MingYang 16 MW and Bewind 14 MW medium-speed drivetrains, and GE Haliade 14 MW and Siemens Gamesa 14 MW direct-drive solutions, which shows that there is no single solution for the selection of drivetrain configuration for wind turbines with a rated power around 15 MW. Even for geared configurations, there are different choices of gearbox ratio offered by different manufacturers. The next commercially available turbine is expected to have a nominal power of about 20 MW. Due to the significant influence of drivetrain on turbine reliability and availability [10], turbine manufacturers are running extensive simulations and test campaigns to optimize their drivetrain systems for offshore applications. The floating offshore application can expose turbines to a wider range of external excitation frequencies and the risk of unknown dynamics, which could be critical for drivetrain operation. As explained in [11–13], higher efficiency and reliability, less maintenance costs and less downtime, due to compactness and lightweight design, and the elimination of brushes, are all motivations for using PMSG in the drivetrain of high-power offshore wind turbines.

Moghadam et al. in [11] proposed a life cycle assessment approach by taking, simultaneously, into consideration the drivetrain design, manufacturing and operation and maintenance (O&M), to examine the pros and cons of three different drivetrain technologies based on direct-drive, medium- and high-speed PMSGs for 10 MW wind turbines. In that paper, the authors reported that the selection of drivetrain topology depends on the power and application, and cannot be extended to different turbines of different powers and applications. By moving from 10 MW to 15 MW, one can still see different choices in the drivetrain configuration in industry. In theory, the output coefficient of an electric generator is  $K \propto \frac{P}{V \cdot N}$  [14], where  $P$  is the nominal power,  $V$  is the volume ( $V = D^2 L$ , with  $D$  the diameter and  $L$  the length) and  $N$  is the rotational speed. Therefore, to maintain the output coefficient at lower rated rotational speeds of the generator (toward direct-drive configuration), the volume of the generator has to increase. The latter shows why direct-drive generators are designed and constructed to have large diameters. This relationship also shows that, by moving toward larger turbines and higher powers, due to reduction of the rotational speed to maintain the tip speed ratio, the generator volume and mass increases more than linearly.

Comparing the different drivetrain technologies from the different aspects of design, manufacturing and O&M attracted the attention of the research society and industry. Li et al. in [15] performed a study on a 1.5 MW wind turbine drivetrain, based on PMSG, and demonstrated how increase in the gear ratio of the gearbox could influence the generator's active material weight and cost. Harzendorf et al. in [16] focused on operational behavior and the criterion called drivetrain-influenced unplanned operational effort (DUOE). The authors compared five different concepts of drivetrain, based on direct-drive and gearbox, with two different types of generators, doubly-fed induction generator (DFIG) and PMSG, for a rated power of 3 MW and showed that the direct-drive concept, based on PMSG, led to the lowest mean DUOE over the drivetrain's lifetime. A holistic comparison between a wide range of drivetrain concepts is given by the same authors in [17]. Authors in [11] compared the direct-drive, medium- and high-speed PMSG-based drivetrain configurations for a 10 MW wind turbine by looking into performance these different drivetrain technologies and considering the design, manufacturing and O&M phases of drivetrain operation. The results of this study showed that the reduced weight of drivetrain, due to a smaller generator, can compensate for the increased weight, due to the presence of the gearbox, in geared drivetrain technologies. That study also cast doubt on the judgement that gearbox

removal in the direct-drive technology could improve the overall efficiency and reliability of the drivetrain. Recent research carried out by Jenkins et al. in [18] compared the medium-speed and direct-drive PMSG-based drivetrain technologies for 15 MW wind turbine drivetrain from the O&M perspective and the reported results were complementary to the study performed in [11]. The results of that study, by taking into account the generator, gearbox and rotor blades, showed that the total O&M cost (vessel + repair + lost electricity costs) of the medium-speed technology could be lower than direct-drive over the turbine lifetime driven by the lower repair cost, despite a larger number of replacements.

The emphasis of this paper is on the coupled gearbox-generator design for direct-drive, medium- and high-speed drivetrain realizations for 15 MW bottom-fixed and floating offshore wind turbines applications. This paper aimed to show how the choice of the gearbox of the drivetrain in 15 MW turbines can influence the overall drivetrain cost and performance by using a life cycle assessment approach.

The main contributions of this research are:

- The conceptual design of the 15 MW drivetrain of three different topologies, namely direct-drive, medium- and high-speed drivetrain systems is presented,
- The three PMSG-based drivetrain systems, designed for 15 MW offshore wind turbines, are compared from weight, dimension, efficiency and raw material cost perspectives,
- The feasibility of the three designed drivetrain systems is evaluated by performing a drivetrain and turbine coupled dynamic analysis in OpenFAST and exposing the turbines to turbulent wind and irregular wave conditions for both bottom-fixed and floating offshore applications,
- Compared to the previous work [11], a more accurate model of drivetrain weight is presented, which helps to achieve a more reliable comparison between the different drivetrain configurations.

The following assumptions were made in this work:

- Even though the designs of the main components are based on optimization, the drivetrain system level optimization, to find the optimal gearbox ratio for each of the medium- and high-speed drivetrain technologies, is beyond the scope of this paper,
- The different bedplate, main bearing housing, low-speed coupling and converter requirements, due to different voltage levels, can also contribute to the weight comparison of the different drivetrain configurations, which are not taken into consideration in the comparison studies,
- The higher voltage level in geared technologies reduces the size of the transformer and facilitates its placement in the bottom of the tower, which is not taken into account.

This paper is structured as follows. In Section 2, the methodology, including the drivetrain life cycle assessment approach, the internal generator and gearbox optimized design approaches and the drivetrain dynamic model, are discussed. In Section 3, the generator and gearbox optimization results of the three drivetrain configurations under consideration, the dynamic analysis of each drivetrain technology, and the comparison study between the different drivetrain systems are presented. This work is finally concluded in Section 4.

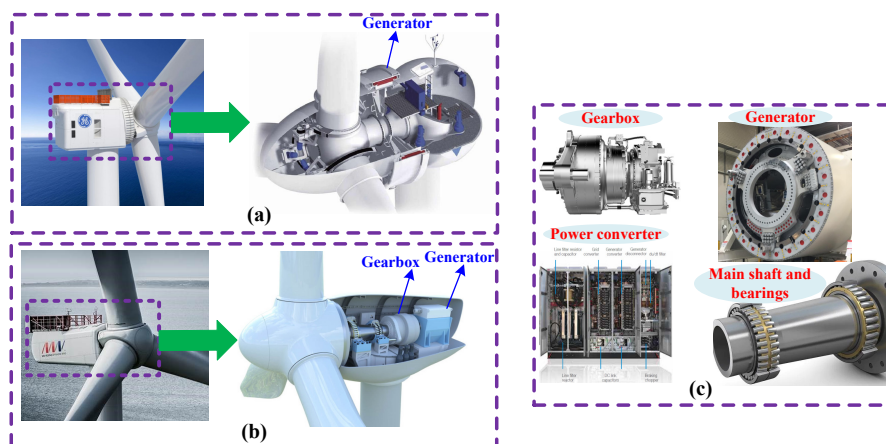


**Figure 1.** Drivetrain configurations and main components. (a) Direct-drive drivetrain, (b) Geared drivetrain, (c) Drivetrain breakdown (photos and figures are adopted from [19–26]).

## 2. Methodology

As discussed in [11], the choice of gearbox can significantly influence the overall weight, dynamic behavior, efficiency, manufacturing, installation, maintenance, reliability and availability of the drivetrain. In this section, to provide the framework required to compare the different drivetrain concepts for 15 MW offshore wind turbine application, the conceptual design at the component-level in each configuration is explained. The main focus is on the generator and gearbox coupled design. The interactions between generator and gearbox design in the drivetrain are discussed in [11]. The three drivetrain configurations under consideration are based on direct-drive, medium- and high-speed generators. We initially followed a similar approach in the generator and gearbox optimized design and validation as that proposed by [11] for a 10 MW drivetrain, with adjustments in the design strategy, according to the requirements of a 15 MW drivetrain design. Additional details were added to this model, which are explained below.

### 2.1. Drivetrain Life Cycle Assessment

Drivetrain life cycle assessment is based on simultaneously considering the feasibility and complexity of design, raw material and manufacturing costs, installation efforts, the costs of O&M, life extension and decommissioning phases of the drivetrain operation.

In this work, life extension and decommissioning were not taken into consideration. In regard to the design consideration in the drivetrain life cycle assessment, the dynamic models of the different drivetrain technologies were constructed, and the possibility of resonance between the drivetrain natural frequencies and the external excitation frequencies, due to the coupled effects of wind, wave and structurally-induced motion natural periods, and structural modes, were investigated. The dynamic properties and behavior of the drivetrain is generally an important factor in the comparison of the different possible drivetrain realizations.

To consider the role of manufacturing in the life cycle assessment, the raw material consumption of the different configurations was examined. For this purpose, the weight and size of the different drivetrain technologies were specified by solving the component-level raw material cost minimization problems of the generator and gearbox as the two main contributors to the overall drivetrain weight. The latter also provides input to calculate the installation costs (transport and craning operations), but this was not studied in this work. The length and diameter of the drivetrain components have an influence on the nacelle and bedplate size, which both influence the nacelle overall weight and, therefore, the manufacturing and installation costs. Weight is critical as it influences the installation and service costs, because a heavier drivetrain or nacelle requires more costly lifting operations. The drivetrain manufacturing costs are correlated to the drivetrain weight, but different drivetrain topologies, and the selection of components, can have a different ratio of raw

material cost to overall drivetrain weight. The reason for this is that the cost to weight ratio of generators and gearboxes is dependent on their design complexity, and size has a different magnitude. Additionally, even inside a component, there is not necessarily a constant cost to weight ratio for different topologies. The gearbox manufacturing costs are closely connected to the gearbox weight; but not, however, necessarily proportional. This is because different machine elements have different cost to weight ratios and, therefore, different gearbox configurations can have different ratios of raw material costs to overall gearbox weight. As discussed earlier, the complexity of the drivetrain influences the design and manufacturing costs, as well as the maintenance and, hence, the operational costs. The use of standard parts is always the goal, as this reduces the design and manufacturing costs. However, the design process within the extent of this work is not detailed enough to make a differentiated assessment of the ability to use standard parts of the different drivetrain technologies. For all these reasons and, also, the uncertainties in the unit costs of materials, the cost of raw material was not used as a key performance index in the overall drivetrain comparison study. The cost of raw material is discussed in the paper as each component was individually designed to minimize the raw material costs.

The life cycle assessment should also accommodate O&M costs. The drivetrain efficiency is important to the overall cost of energy. The overall efficiency of the different drivetrain configurations was one of the criteria considered here to account for operation in the life cycle assessment. Reliability has a key influence on the maintenance and, therefore, the operational expenditure. It also has an impact on the lifetime and, therefore, influences the LCOE. The reliability analysis of the drivetrain can be performed by using long-term fatigue damage analysis of the bearings and gears as the drivetrain fatigue damage critical components, which should be profoundly inspected against the fatigue defects. Then, the damage index can be defined as the indicator of the overall fatigue damage for each drivetrain technology, by following the procedure explained in [1], and using the bearings and gears specification as a result of this study. The latter can be supported by machine learning to account for the model and measurement uncertainties [27]. This work provides the specification of the drivetrain components as the main input for a detailed reliability analysis. To maintain the tip speed ratio of larger rotors in higher powers to reach the highest power coefficient, the nominal rotational speed of rotor is reduced. The latter, together with the different selection of drivetrain, turbine and support substructure components, are the reasons why a failure modes analysis for a drivetrain of a similar technology would not be valid when the rated power, rotational speed and support substructure change. Therefore, an analysis for the 15 MW turbine, in particular, was performed in this work.

## 2.2. Drivetrain Layout

Different drivetrain layouts for rotor–gearbox–generator configuration, based on both direct-drive and geared drivetrain technologies, are described in [28]. Figure 2 illustrates the two different drivetrain layouts assumed for the geared and direct-drive drivetrain configurations in this research. The two geared drivetrain technologies, based on medium- and high-speed generators, are assumed to be based on a four-point suspension and two main bearings. In this layout, a second main bearing is placed right before the gearbox at the end of the main shaft to react to the non-torque loads right before the gearbox (Figure 2a). The direct-drive drivetrain is based on a double main bearings design, where the bearings are integrated to the hub and are outer ring/race rotating bearings (Figure 2b).

The distribution of loads, the size and weight of the two main bearings and the requirements of the main bearings housing are different in these two different drivetrain layouts. For example, in the direct-drive drivetrain layout, there is no need to use additional housings for the two main bearings, which can reduce the overall drivetrain weight.



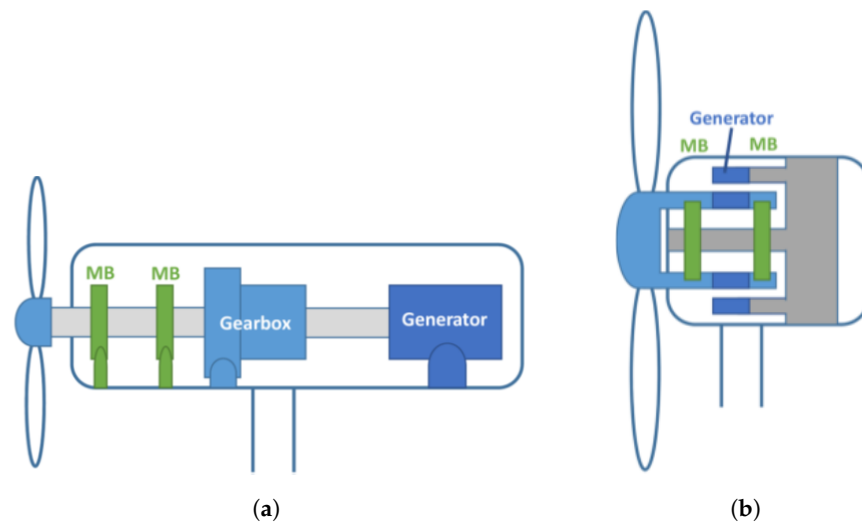


**Figure 2.** Drivetrain layout assumed for the drivetrain technologies under consideration in this paper (adopted from [28]). (a) Four-point suspension (geared), (b) Three-point suspension (direct-drive).

### 2.3. Generator Design

In wind power applications, the most common large permanent magnet generator for direct-drive is the outer rotor radial-flux surface mounted PMSG, and the most common for the geared drivetrain is the same technology, but with an inner rotor. The main advantages with inner and outer rotor radial-flux PMSGs, when compared to one another, are discussed in [29]. The area covered by a single pole for the three designed generators are depicted in Figure 3, which shows the stator windings placed in the stator slots, the stator and rotor cores and the permanent magnets placed on the rotor surface.

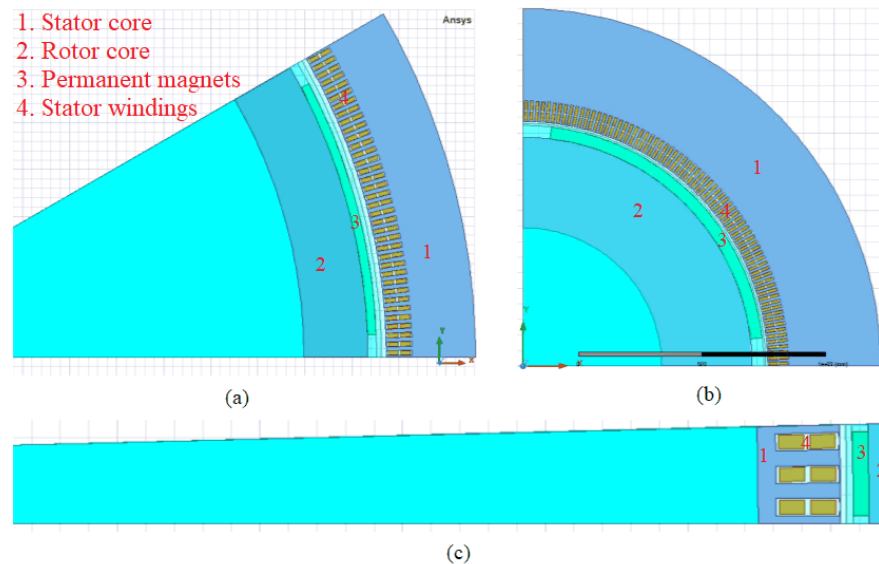


**Figure 3.** PMSG layout. (a) medium-speed (inner rotor), (b) high-speed (inner rotor), (c) direct-drive (outer rotor).

The cost function applied to the generator optimized design problem was the cost of active material over the torque density, as defined by [11], and aimed at maximizing the utilization of generator weight. The optimization problem was the function of five design variables, namely, the air-gap diameter  $D_s$ , stack length  $L_s$ , slot width  $b_s$ , slot height  $h_s$  and magnet height  $h_m$ . The design constraints included the equality constraint, related to the no-load Electromotive force (emf), and inequality constraints, related to the limits of current density. The proper mechanical design to withstand vibration and bending (slot height

to width, slot width to tooth width, magnet height to pole pitch and air-gap diameter to stack length ratios), the limits of tooth and air-gap flux densities, and the specific electrical loading were added to the design objective function. The main optimization constraints, as the function of the five optimization variables, are described by the following equation:

$$\text{induced voltage: } \sqrt{2}k_w n_r \frac{2\pi}{60} \frac{N}{3} \frac{D_s}{2} L_s B_r \frac{h_m}{\mu_{pm} \frac{\pi D_s}{Q} - \frac{b_s}{5(\delta + \frac{h_m}{\mu_{pm}})} + b_s} (\delta + \frac{h_m}{\mu_{pm}}) \frac{4}{\pi} \sin\left(\frac{\pi}{2} \frac{b_m}{\tau_p}\right), \quad (1a)$$

$$\text{current density: } \frac{3V_{ph}(b_s - 2h_i)(h_s - h_w - 4h_i)}{P_e Q}, \quad (1b)$$

$$\text{magnet height to pole pitch ratio: } \frac{h_m + \delta}{\frac{\pi D_s}{p}}, \quad (1c)$$

$$\text{tooth height to width ratio: } \frac{h_s}{\frac{\pi D_s}{Q} - b_s}, \quad (1d)$$

$$\text{slot width to tooth width ratio: } \frac{b_s}{\frac{\pi D_s}{Q} - b_s}, \quad (1e)$$

$$\text{tooth flux density: } B_r \frac{h_m}{\mu_{pm} \frac{\pi D_s}{Q} - \frac{b_s}{5(\delta + \frac{h_m}{\mu_{pm}})} + b_s} (\delta + \frac{h_m}{\mu_{pm}}) \frac{4}{\pi} \sin\left(\frac{\pi}{2} \frac{b_m}{\tau_p}\right) \frac{\pi D_s}{Q} \frac{(L_s + 2\delta)}{(\frac{\pi D_s}{Q} - b_s) k_{fe} L_s}, \quad (1f)$$

$$\text{air-gap flux density: } B_r \frac{h_m}{\mu_{pm} \frac{\pi D_s}{Q} - \frac{b_s}{5(\delta + \frac{h_m}{\mu_{pm}})} + b_s} (\delta + \frac{h_m}{\mu_{pm}}) \frac{4}{\pi} \sin\left(\frac{\pi}{2} \frac{b_m}{\tau_p}\right), \quad (1g)$$

$$\text{electric loading: } \sqrt{2}P_e \frac{\mu_{pm}}{\pi^2 k_w A^{max} \frac{n_r}{60} B_r \frac{4}{\pi} \sin\left(\frac{\pi}{2} \frac{b_m}{\tau_p}\right)} - \frac{D_s^2 L_s h_m}{\left(\frac{\pi D_s}{Q} - \frac{b_s}{5(\delta + \frac{h_m}{\mu_{pm}})} + b_s\right) (\delta + \frac{h_m}{\mu_{pm}})}, \quad (1h)$$

where  $k_w$  is the winding factor. The definition of the other parameters are given in Section 3.2.

The direct relationship between the induced voltage and speed, means that, by taking into consideration the rotational speed in the direct-drive compared to medium-speed, the medium-speed compared to high-speed generator is reduced, and it is not efficient to design these generators with the same voltage level. As a result, to realize a more realistic design, these generators were designed for different standard voltage levels, which also helped to significantly save in the overall weight of the designed generators.

The conceptual design performed by using this analytical design approach was then modeled and validated using Ansys RMxprt to ensure that the designed generator was able to stably deliver the desired power at the desired voltage level. In this model, more details of the slots, material properties and the windings were applied, which caused the design outputs to slightly change compared to the primary input values calculated from the conceptual design step.

In this work, compared to the generator design proposed in [11], a detailed model of structural weight was employed to realize a more accurate comparison between the total weight of the different generators under consideration. The generator structural model is described in the following.

*Structural model of PMSG:* The generator structural model of radial-flux permanent magnet machines was adopted from [30], where a disc structure was used for the rotor and an arm structure with hollow arms for the stator. The design criteria were the deflections (radial, axial and torsional) to maintain the air-gap clearance against the structural forces

acting on the structure and torque limitations, as explained by [31]. By using this model, the generator structural weight is described by the equation:

$$m_{str} = m_{str}^{rot} + m_{str}^{stator} + m_{bearings}, \quad (2a)$$

$$m_{str}^{rot} = m_{disk} + m_{cylinder}^{rot} + m_{shaft}, \quad (2b)$$

$$m_{str}^{stator} = m_{arms} + m_{cylinder}^{stator}, \quad (2c)$$

where  $m_{str}^{rot}$ ,  $m_{str}^{stator}$  and  $m_{bearings}$  are the structural weight of rotor, the structural weight of stator and the weight of generator bearings, respectively.  $m_{disk}$  and  $m_{cylinder}^{rot}$  are the weights of rotor support disk and cylinder, and  $m_{shaft}$  is the weight of generator shaft.  $m_{arms}$  and  $m_{cylinder}^{stator}$  are the weights of the support arms and cylinder of stator. The weight of generator bearings and shaft was not included in the calculation of the structural weight of the direct-drive generator, because the main bearings and main shaft were not included in the weight calculations of the three drivetrain technologies under consideration. Moreover, the arm structure was assumed to be used for both the rotor and the stator of the outer rotor direct-drive generator. The generator shaft was roughly designed based on the maximum torsional stress, the stiffness requirements to limit the shaft deflection, and the diameter requirement to match the bore diameter of the deep groove roller bearings of the generator. The cooling system design of the generator was generally performed in a way to keep the generator size down and to ensure that the operation of the generator was within the safe thermal limits [32]. The cooling system design and its influence on the structural weight was not considered here.

One main source of mechanical vibrations in PMSGs is the cogging torque. The attractive force between rotor magnets and steel-made stator slots which is called cogging effect is prevalent in slotted synchronous motors. The oscillatory torque generated by the generator to oppose the cogging effect is called the cogging torque. As the definition says, the fundamental cogging frequency  $f_{cog}$  is the function of the number of rotor poles  $P$  and stator slots  $Q$  as defined by:

$$f_{cog} = \frac{Q}{p} f_s. \quad (3)$$

By taking into consideration that in each rotation,  $p$  poles interact with  $Q$  slots, the resultant cogging torque is made of a modulated carrier with the frequency  $f_{cog}$  modulated by a signal with the frequency  $2f_s$  [33]. Different analytical models are proposed in the literature for modeling the cogging torque [34]. A common way to model cogging torque is based on the energy approach. In this method, cogging torque is derived from the magnetic flux density spatial distribution by calculating the rate of change of total stored energy in the air-gap with respect to the rotor angular position assuming the energy variation in the iron is negligible compared with the energy variation in the air-gap [33,35]. The latter leads to Equation (4) as

$$T_{e-cog} = \frac{dW}{d\theta} = \frac{gL_e D_s}{4\mu_0} \frac{d}{dx} \int_0^\tau b_g(x)^2 dx, \quad (4)$$

where  $g$  is the mechanical air-gap height,  $L_e$  is the effective length of stator core,  $\mu_0$  is the air-gap permeance,  $\tau$  is rotor pole pitch described by  $\tau = \frac{\pi D_s}{p}$ ,  $D_s$  is air-gap diameter and  $b_g(x)$  is the air-gap magnetic flux density expressed as a function of the  $x$  coordinate representing the linear displacement of rotor in the air-gap.  $b_g(x)$  further depends on the maximum value of the stator current, the winding factor and the number of stator turns in series in each phase. In the above model, the cogging torque of a single pole was analyzed, which could be extended to the other poles.



## 2.4. Gearbox Design

### 2.4.1. Gearbox Configuration and Layout

The decision on the gearbox configuration was a compromise between weight, complexity and efficiency. One of the most common gearbox configurations in offshore wind turbines, to realize medium-speed and high-speed drivetrain technologies, is a conventional three-stage configuration with two planetary stages and one parallel stage [36–38]. Depending on the overall gear ratio, three planetary stages could be a better solution considering the overall weight reduction [11]. This topology was also the one used by MHI Vestas in V236-15.0 MW wind turbine [39]. Using a planetary stage, compared to parallel, helps to keep the torque–density up, even if it costs more to manufacture. A comparison between the gearbox with two planetary stages and one parallel stage and three planetary stages to realize the 15 MW medium-speed drivetrain is given in [40]. In general, the gearbox mass has a relationship with the rated rotor torque in such a way that it increases as the torque increases. The increase of torque happens in the case that the rated power of the turbine increases, or the rated rotor speed decreases, which both these cases happen simultaneously when sizing up a turbine from 10 to 15 MW.

The study performed by Desch [40] showed that a four-stage gearbox was a promising configuration for the high-speed drivetrain, from the weight and raw material cost points of view. Therefore, a four-stages gearbox configuration was considered for the high-speed drivetrain analysis in this work.

An individual gear stage has an optimal stage ratio for which the relation between the achieved gear ratio and the gear weight reaches a minimum value [41,42]. This is the reason why the optimal number of stages increases with the increased gearbox overall ratio. This assumption could justify the view that a fourth stage only has benefits for a high-speed gearbox as the gearbox ratio of this gearbox is much higher than that in a medium-speed gearbox.

A planetary stage with fixed ring gear, driving planetary carrier and driven sun gear was used. Five planets in the first stage and three planets in all the following stages, as used in [11,38], were assumed in the planetary stages. This configuration was still found to be reasonable for 15 MW, because the increase of the planet number in the following stages was shown to reduce the gearbox weight by 1 to 2% but had no significant influence on the overall comparison [40]. Therefore, the optimization of the number of the planets of each stage was not of a focus in this work. The bearing arrangement was chosen according to the recommendations in IEC 61400-4 [43]. According to the chosen bearings types and the static loads, the size of the bearings was calculated by using KISSsoft to reach a lifetime of 20 years.

### 2.4.2. Gearbox Optimization

As discussed earlier, the main factors for the gear weight of a gear stage are the torque and the stage ratio. The optimized gearbox design consisted of a conceptual design step, using an analytical gearbox model to find the optimized gear ratios of the stages in the gearbox layout, and a detailed design step, using KISSsoft software to obtain the detailed geometry of gears, their equivalent model parameters, including inertia and stiffness, their weights and the overall performance indices, such as efficiency. The details of the gearbox shafts and bearings could also be specified in this analysis. The gearbox model used for the 15 MW gearbox design optimization was based on [44], and, throughout this section, the gearbox optimized design code [45] was used. The authors remind the reader that the Matlab implementation of the gearbox design code is available online [45]. The objective function of the gearbox optimization algorithm is the minimization of the gears' overall weight by optimizing the gear stage ratios. This optimization is based on the gear stage weight model proposed by [44], which contains the correlation between the gear weight of an individual stage and the stage ratio on a physical basis.

The weights of a planetary  $m_{\text{gear}}^{\text{planetary}}$  and a parallel stage  $m_{\text{gear}}^{\text{parallel}}$  are calculated as the function of the torque of the individual stage  $Q_S$ , the gear stage ratio  $u$  and the planets number  $B$  for a planetary stage [44] as:

$$m_{\text{gear}}^{\text{planetary}} = \frac{2\rho_{\text{Fe}}Q_S}{k} \left( \frac{1}{B} + \frac{1}{B(\frac{u}{2} - 1)} + (\frac{u}{2} - 1) + (\frac{u}{2} - 1)^2 + k_r \frac{(u - 1)^2}{B} + k_r \frac{(u - 1)^2}{B(\frac{u}{2} - 1)} \right), \quad (5)$$

$$m_{\text{gear}}^{\text{parallel}} = \frac{2\rho_{\text{Fe}}Q_S}{k} \left( 1 + \frac{1}{u} + u + u^2 \right), \quad (6)$$

where  $\rho_{\text{Fe}}$  is the density of steel,  $k$  is the intensity of the tooth loads factor and  $k_r$  is the ring scaling factor. The input torque of the individual stage  $S$ , defined as  $Q_S$ , can be expressed as a function of the rated input torque  $T_N$  and the individual gear stage ratios of the previous stages  $u_i$ :

$$Q_S = \frac{T_N}{\prod_{i=1}^{S-1} u_i}. \quad (7)$$

The total gears weight of the gearbox with  $k$  planetary and  $l$  parallel stages is  $m_{\text{gear}}^{\text{GB}}$ :

$$m_{\text{gear}}^{\text{GB}} = \sum_{i=1}^k m_{\text{gear},i}^{\text{planetary}} + \sum_{i=1}^l m_{\text{gear},i}^{\text{parallel}}, \quad (8)$$

which is the sum of the weight of all the individual stages.

This optimization problem in Equation (8) was solved by using Matlab `fmincon` nonlinear optimization solver. The inputs were the gearbox configuration (number and type of stages), the rated torque, the overall gear ratio, the number of planets in the planetary stage and a constraint related to the gear ratio of each stage. The outputs were the optimized stage ratios and the calculated weight. In [11], a weight correction factor was used to account for the weight of bearings, shafts, housing and lubrication. In this work, a more accurate weight model of gearbox was used. For this purpose, KISSsoft was used to size the shafts and bearings and to calculate the weight of bearings and shafts, while the weight of housing and lubrication was not taken into consideration in the reported overall gearbox weight. With the optimized gear stage ratios, a detailed gearbox design in KISSsoft was conducted.

The total gearbox weight  $m_{\text{GB}}$  including gears, shafts and bearings was:

$$m_{\text{GB}} = \sum_{i=1}^S \left( m_{\text{gear},i}^{\text{planetary}} + m_{\text{gear},i}^{\text{parallel}} + m_{\text{shafts},i} + m_{\text{bearings},i} \right). \quad (9)$$

The gearbox raw material costs were calculated in KISSsoft, using the weights of the different components (shafts, gears, bearings) and the predefined cost factors to calculate an estimate for the costs of the different machine elements, based on their weight. The gearbox raw material cost  $C_{\text{GB}}$  was:

$$C_{\text{GB}} = \sum_{i=1}^S \left( c_{\text{gear}} \cdot m_{\text{gear},i}^{\text{planetary}} + c_{\text{gear}} \cdot m_{\text{gear},i}^{\text{parallel}} + c_{\text{shafts}} \cdot m_{\text{shafts},i} + c_{\text{bearings}} \cdot m_{\text{bearings},i} \right). \quad (10)$$

The cost factors  $c$  of the different gearbox components used in the Equation (10) were defined in Section 3.3.

### 2.5. Drivetrain Dynamic Analysis

The general form of n-DOF torsional dynamic model of drivetrain in the time domain was defined by [18]:

$$\mathbf{J}\ddot{\boldsymbol{\theta}}(t) + \mathbf{C}\dot{\boldsymbol{\theta}}(t) + \mathbf{K}\boldsymbol{\theta}(t) = \mathbf{q}(t), \quad (11)$$

where  $\mathbf{J}$ ,  $\mathbf{C}$  and  $\mathbf{K}$  are the moment of inertia, damping and stiffness matrices with the size  $n \times n$ .  $\boldsymbol{\theta}$  and  $\mathbf{q}$  are the response and load vectors with the size  $n \times 1$ . The procedure to calculate the inertia and stiffness matrices from the geometrical and material properties of the drivetrain are explained in [46]. The torsional natural frequencies by using this model can be calculated by:

$$\omega_i \text{ (for } i = 1, \dots, n) = \sqrt{\text{eig}(-\mathbf{J}^{-1}\mathbf{K})}. \quad (12)$$

To see the influence of gearbox inertia on the drivetrain dynamics, the equivalent gearbox inertia was calculated from the equivalent inertia of each stage by using the equation:

$$I_{gear}^{MS} = \frac{1}{\frac{1}{I_{s1}} + \frac{1}{\alpha_1 I_{s2}} + \frac{1}{\alpha_1 \alpha_2 I_{s3}}}, \quad (13a)$$

$$I_{gear}^{HS} = \frac{1}{\frac{1}{I_{s1}} + \frac{1}{\alpha_1 I_{s2}} + \frac{1}{\alpha_1 \alpha_2 I_{s3}} + \frac{1}{\alpha_1 \alpha_2 \alpha_3 I_{s4}}}, \quad (13b)$$

where  $I_{si}, i \in 1 - 4$ , is the equivalent inertia of the gear stage  $si$  from the the stage input shaft, and  $\alpha_i$  is the gear stage ratio. To estimate the generator inertia for the dynamic model, one can use the equation:

$$I_{gen} = I_{rot-yoke} + I_{PM} + I_{shaft} + I_{cylinder} + I_{disk} + I_{shaft}, \quad (14)$$

where  $I_{rot-yoke}$ ,  $I_{PM}$ ,  $I_{shaft}$ ,  $I_{cylinder}$ ,  $I_{disk}$  and  $I_{shaft}$  are the inertia of the rotor yoke, permanent magnets, support cylinder, support disk and shaft, respectively. To estimate the high-speed shaft stiffness for the dynamic model, the following equation can be used:

$$k^{HSS} = k_{gear}^{shaft} + k_{coupling} + k_{gen}^{shaft}, \quad (15)$$

where  $k_{gear}^{shaft}$  is the stiffness of the part of gearbox shaft placed between the gearbox output and the coupling,  $k_{coupling}$  is the stiffness of the coupling, and  $k_{gen}^{shaft}$  is the stiffness of the part of generator shaft placed between the generator output and the coupling. The length of gearbox and generator output shafts were selected to fit the coupling and to leave some space for instrumentation and maintenance operations. The criteria for the selection of generator coupling in geared drivetrain technologies were the high torque capacity, low torsional flexibility, backlash free and fail safe features and the possibility to add the disk brake. The coupling torque was selected based on the rated and peak torques of the driving side and the applying of sufficient safety factors.

To analyze the turbine-power train systems coupled dynamics in the three drivetrain configurations under consideration, the equivalent reduced-order dynamic model of each drivetrain configuration was created. Then, the drivetrain equivalent dynamic models were integrated into the turbine simulations containing both the turbine model and the external loads. As a result, the drivetrain loads were calculated from the fully-coupled turbine-power train dynamic model. The turbine model developed in NREL's OpenFAST is a detailed coupled aero-hydro-servo elastic dynamic model, which contains the structural and power train dynamics loading NREL Reference OpenSource Controller (ROSCO). More details about OpenFAST load and response analysis can be found in [47]. The global simulations were performed for both bottom-fixed monopile and floating semi-submersible (UMaine design) substructures. This model was beneficial from two aspects. First, to validate the drivetrain design, by using the coupled turbine model, to show that resonance avoidance could be achieved in each of the designs for different operating conditions and to ensure a safe operation for all the load cases defined by IEC61400-1 standard [48]. Second, to calculate the accurate values of the drivetrain loads for various load cases to provide the inputs for potential drivetrain life calculation and reliability analysis.

The power train model in the global simulations was a two-degree-of-freedom (2-DOF) torsional model, which was able to capture the dynamics due to the first power train system rigid and non-rigid modes and their interactions with the structural modes and external excitation sources. The following equation describes the first rigid and nonrigid torsional natural frequencies of the general case of geared drivetrain based on a 2-DOF model as:

$$f_1^{tor-nonrigid} = \frac{1}{2\pi} \sqrt{\frac{\alpha^2 k_r k_{gen}}{k_r + \alpha^2 k_{gen}} \frac{J_r + \alpha^2 J_{gen}}{\alpha^2 J_r J_{gen}}}, \quad (16a)$$

$$f_1^{tor-rigid} = \frac{1}{2\pi} \sqrt{\frac{k_{eq}}{(J_r + \alpha^2 J_{gen})}}, \quad (16b)$$

where  $J_r$  and  $J_{gen}$  are the moment of inertia of rotor and generator,  $k_r$  and  $k_{gen}$  are the stiffness of the main- and high-speed shafts, respectively.  $\alpha$  is the inverse of the overall gear-ratio which takes the value 1 for the direct-drive drivetrain. Gear-ratio in IEC 61400-4 is defined by  $\frac{n}{n_r}$ , where  $n$  and  $n_r$  are the rotational speeds of the input and output shafts, respectively [43].  $k_{eq}$  is the equivalent stiffness presented by the rotor-generator system interacting between this system and nacelle.

### 3. Results and Discussions

#### 3.1. Case Study

In this study, the IEA 15 MW reference wind turbine, simulated in OpenFAST, was used, and the three 15 MW drivetrain concepts, based on direct-drive, medium- and high-speed generators, were designed and tested, coupled with this turbine model. In the tabulated results in this section, DD, MS and HS stand for the direct-drive, medium- and high-speed technologies, respectively. For the drivetrain dynamic analysis, the drivetrain input loads were calculated from the drivetrain-turbine coupled simulations. The global simulations were performed based on the IEA 15 MW offshore reference wind turbine located on two different support substructures, namely monopile fixed-bottom foundation [49] and the University of Maine semi-submersible floating platform [50]. The input wind field was modeled turbulent and the three dimensional turbulent wind field was modeled by using NREL's TurbSim, where the turbulence model was based on the Kaimal spectrum and the exponential coherence model. IEC turbulence category B and the power production load case, based on the normal turbulence model (NTM), were assumed for designing the turbine simulation cases. In the power production mode, three different environmental conditions were simulated, as listed in Table 1. For different average wind speeds  $U_w$  corresponded to below-rated, rated and above-rated wind speed operations within the operational range of the turbine, the most probable values of turbulence intensity  $I$ , significant wave height  $H_s$  and peak period  $T_p$  were selected in the global simulations, depending on the average wind speed and turbulence category [48,51].

**Table 1.** Environmental conditions for drivetrain analysis.

EC	1	2	3
$U_w$ (m/s)	7	11	15
$I$ (%)	22	18	16
$H_s$ (m)	2.5	3.5	3.5
$T_p$ (s)	6.5	7.5	11.5

#### 3.2. Generator Optimized Design Results

The generator design specification of direct-drive (DDPMSG), medium-speed (MSPMSG) and high-speed (HSPMSG) generators, based on the optimized design approach explained in Section 2.3, is presented in Table 2. The unit costs of raw materials were selected from [52–55].

The unit prices change over the time, but this did not restrict the generator optimized design methodology, though it could change the results of optimization and the estimated raw material costs of the different generators under consideration. SKF 361844 was selected as the medium-speed generator, and SKF 6092 MB was selected as the high-speed generator bearings, which were all deep groove ball bearings. Following the procedure explained in [1], to calculate the reaction forces and select the generator bearings, four of these bearings should be used in each generator to meet the life requirements and the required basic dynamic load rating calculated from the desired life and average dynamic load rating. The main reason for the bearings selection here was for the more accurate estimation of the overall weight. The structural elements were assumed to be made of cast iron. KTR Revolex KX-D 355 standard coupling was selected to connect the gearbox and generator in the medium-speed drivetrain, and KTR Revolex KX-D 240 was selected as the coupling for the high-speed drivetrain technology.

**Table 2.** Generator design results.

Generator Specifications	DDPMSG	MSPMSG	HSPMSG
<b>Technical specification</b>			
Type of rotor	outer	inner	inner
Number of poles $p$	254	12	4
Rated output power $P_e$ (Mw)	15.003	15.005	15.000
Rated input torque $T_N$ (MNm)	19.651	0.302	0.096
Rated rotational speed $n_r$ (rpm)	7.56	480	1497.6
Output rated line voltage RMS $V_L$ (kV)	3.464	10.390	17.320
Rated generator output frequency $f_s$ (Hz)	16.0	48.0	49.9
Efficiency $\eta$ (%)	96.44	98.68	99.21
Specific electric loading $A$ (A/mm)	96.39	79.73	79.52
Armature current density $J_s$ (A/mm <sup>2</sup> )	3.04	3.10	3.85
Armature thermal load (A <sup>2</sup> /mm <sup>3</sup> )	292.91	246.96	306.08
Maximum air-gap flux density $\hat{B}_\delta$ (T)	0.64	0.63	0.80
Maximum magnet flux density $\hat{B}_m$ (T)	0.65	0.69	0.86
Maximum stator teeth flux density $\hat{B}_t$ (T)	1.45	1.86	1.86
Maximum stator yoke flux density $\hat{B}_{sy}$ (T)	1.42	1.55	1.51
Maximum rotor yoke flux density $\hat{B}_{ry}$ (T)	1.44	1.60	1.54
<b>Dimension specification</b>			
Air-gap diameter $D_s$ (m)	14.034	4.289	1.573
Active length $L_s$ (m)	1.407	0.404	0.601
Slot width $b_s$ (mm)	30.3	20.0	10.0
Slot height $h_s$ (mm)	110.2	73.0	64.4
Magnet height $h_m$ (mm)	27.8	28.5	38
Stator yoke height $h_{sy}$ (mm)	33.8	218.0	302.3
Rotor yoke height $h_{ry}$ (mm)	59.0	237.9	328.6
Magnet width $b_m$ (mm)	148.0	940.1	1007.4



Table 2. Cont.

Generator Specifications	DDPMSG	MSPMSG	HSPMSG
number of slots $Q$	762	432	288
Number of slots per pole & phase $q$	1	12	24
Air-gap height $\delta$ (mm)	22	17	13
Pole pitch $\tau_p$ (mm)	173.6	1122.8	1235.0
Wedge height $h_w$ (mm)	1.5	1.5	1.5
Outer diameter $D_{so}$ (m)	14.196	4.871	2.298
Inner diameter $D_{ri}$ (m)	13.746	3.777	0.890
Equivalent core length $L_e$ (m)	1.407	0.404	0.601
Slot pitch $\tau_s$ (mm)	57.9	31.2	17.2
<b>Winding specification</b>			
winding layers	2	2	2
Winding type	full pitch	full pitch	full pitch
Parallel branches	1	1	1
Conductors per slot	2	2	2
Winding connection	star	star	star
Number of winding turns $N$	600	432	288
Insulation thickness $h_i$	1 mm/kv	1 mm/kv	1 mm/kv
<b>Material properties</b>			
Magnet Material	NdFe35	NdFe35	NdFe35
Magnet density $\rho_{pm}$ (kg/m <sup>3</sup> )	7400	7400	7400
Relative permeability of magnet $\mu_{pm}$	1.1	1.1	1.1
Magnet residual flux density $B_r$	1.23	1.23	1.23
Magnet specific cost $c_{pm}$ (€/kg)	63	63	63
Laminated core Material	M27 24G	M27 24G	M27 24G
Laminated core density $\rho_{fe}$ (kg/m <sup>3</sup> )	7650	7650	7650
Relative permeability	B-H curve	B-H curve	B-H curve
Laminated core specific cost $c_{fe}$ (€/kg)	2.5	2.5	2.5
Copper density $\rho_{cu}$ (kg/m <sup>3</sup> )	8900	8900	8900
Copper specific cost $c_{cu}$ (€/kg)	8.3	8.3	8.3
Cast iron density $\rho_{cu}$ (kg/m <sup>3</sup> )	8900	8900	8900
Cast iron cost $c_{cu}$ (€/kg)	1.3	1.3	1.3
<b>Design parameters</b>			
Core stacking factor $k_{fe}$	0.97	0.97	0.97
Magnetic pole embrace ( $\frac{b_m}{\tau_p}$ )	0.85	0.85	0.85
<b>Mechanical vibrations</b>			
Cogging torque frequency (Hz)	48	1728	3593
Cogging torque (Nm)	3185.67	1.13	0.51

Table 2. Cont.

Generator Specifications	DDPMSG	MSPMSG	HSPMSG
<b>Weight and cost specification</b>			
Armature copper weight $M_{cu}$ (ton)	20.466	5.842	1.966
Permanent magnet weight $M_M$ (ton)	10.904	0.961	0.681
stator core weight $M_{fe}$ (ton)	38.785	10.642	8.997
Rotor core weight $M_{fe}$ (ton)	14.497	7.860	4.807
Total active material weight $M_{Active}$ (ton)	84.653	25.306	16.451
Approximated structure weight $M_{structure}$ (ton)	100.630	32.250	16.695
Total weight $M_{tot}$ (ton)	185.283	57.556	33.146
Total active material cost $c_{Active}$ (M€)	0.99	0.16	0.09
Total raw material cost $c_{total}$ (M€)	1.12	0.20	0.11

The validation of the designed generators was carried out by using the ANSYS RMxprt electrical machines design tool, to ensure that the designed generators were able to deliver the designed power at the desired voltage and frequency. The generators' characteristic curves, namely the power–angle and voltage characteristics, are demonstrated in Figure 4, which shows that the three designed generators could stably deliver the design power at the design voltage. As apparent from this figure, the rated operating point 15 MW in the three designed generators had a safe distance from the power angle stability limit  $\delta = \frac{\pi}{2}$  rad. The designed DDPMSG, compared to HSPMSG, and HSPMSG, compared to MSPMSG, were able to deliver higher powers than the rated designed power.

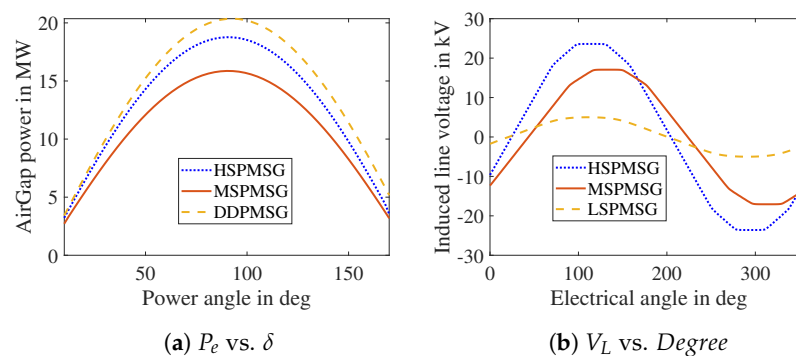


Figure 4. Characteristic curves of the designed generators.

### 3.3. Gearbox Optimized Design Results

The inputs to the gearbox design optimization problem are listed in Table 3. These inputs resulted from the turbine specifications and the generator design. The gear ratios of the medium- and high-speed drivetrain systems in the DTU 10 MW design were 1:50 and 1:156, respectively. By taking into account that the rated rotor speed changed from 9.6 rpm in the 10 MW wind turbine to 7.56 rpm in the 15 MW turbine, the gear ratio of the 15 MW medium-speed drivetrain changed from 1:50 in the 10 MW to 1:63.5 in the 15 MW drivetrain. With a similar explanation, the gear ratio of the 10 MW high-speed drivetrain, proposed by [11], changed from 1:156 in the 10 MW to 1:198.1 in the 15 MW drivetrain. By means of this scaling of the gear ratio, the input speed of the 15 MW generators would be the same as the 10 MW, which helped the input rated generator speed to be in a similar range with the other commercially available medium- and high-speed wind turbine drivetrain systems. It is worth noting that it was possible to realize both the medium- and high-speed drivetrain systems with other gear ratios than what was assumed in this paper.

**Table 3.** Gearbox Specifications.

Gearbox Specifications	MS	HS
Rated input torque $T_N$ (MNm)		18.947
Rated rotational input speed $n_r$ (rpm)		7.56
Overall gear ratio $u$	1:63.5	1:198.1
Density of steel $\rho_{fe}^{gear}$ kg/m <sup>3</sup>	7850	7850
Intensity of tooth loads factor $k$	4,000,000	4,000,000
Ring scaling factor $k_r$	0.4	0.4

Table 4 shows the optimization results of the stage gear ratios, based on the analytical optimized design model presented in Section 2.4.2. These results were the basis for the detailed gearbox design presented below.

**Table 4.** Gearbox stage ratio optimization results.

Gearbox Configuration	MS-3P	HS-3P	HS-3P1H	HS-4P
overall gear ratio	1:63.5	1:198.1	1:198.1	1:198.1
stages	3	3	4	4
planet numbers	5,3,3	5,3,3	5,3,3,-	5,3,3,3
gear ratio stage 1	1:3.3744	1:3.6871	1:3.3618	1:3.2832
gear ratio stage 2	1:3.7495	1:4.904	1:3.7081	1:3.467
gear ratio stage 3	1:5.019	1:10.956	1:4.8126	1:3.689
gear ratio stage 4	-	-	1:1:3.302	1:4.7176

In the simulations in KISSsoft, the pressure angle  $\alpha$  and the helix angle  $\beta$  were assumed to take the values 20° and 0°, respectively. The facewidth  $b$  was roughly sized in the first step, and the module  $m$  and center distance  $a$  were optimized in fine sizing. The shafts were designed for the maximum equivalent Von Mises stress of 180 N/mm<sup>2</sup>, and the bearings were chosen to withstand a lifetime of 20 years.

The design specifications of the optimized medium- and high-speed gearboxes after implementation in KISSsoft are listed in Tables 5 and 6, respectively. As discussed earlier, for the less weight design in the medium-speed drivetrain technology, the gearbox based on three planetary stages was selected, and for the less complex and weight design in the high-speed technology, the gearbox based on three planetary and one parallel stages was selected. The detailed design specifications are given in Tables 5 and 6.

The bearings chosen for the high- and medium-speed drivetrain gearboxes are listed in Tables 7 and 8, respectively. The purpose for the bearing selection was only for the gearbox overall weight estimation and the selected combination might not be optimal from the dynamics point of view.

**Table 5.** Design specifications of MS gearbox based on three planetary stages

Parameter	First Stage	Second Stage	Third Stage
Gear type	Planetary	Planetary	Planetary
Gear ratio	1:3.3696	1:3.75	1:5.0357
Number of planets	5	3	3
Normal module $m$ [mm]	39	35	21
Pressure angle $\alpha$ [°]	20	20	20
Helix angle $\beta$ [°]	0	0	0
Center distance $a$ [mm]	1481	1043	734
Number of teeth, sun $z_s$ [-]	46	32	28
Number of teeth, planet $z_p$ [-]	31	27	41
Number of teeth, ring $z_r$ [-]	109	88	113
Facewidth sun gear $b_s$ [mm]	980	650	450
Facewidth planet gear $b_p$ [mm]	960	630	430
Facewidth ring gear $b_r$ [mm]	980	650	450
Profile shift coefficient, sun $x_s$ [-]	-0.4237	0.1202	0.2755
Profile shift coefficient, planet $x_p$ [-]	-0.0734	0.1910	0.1983
Profile shift coefficient, ring $x_r$ [-]	0.9860	0.4427	0.7198
Weight gears $m_{gear}$ [ton]	52.7	18.9	6.5
Gear mesh efficiency $\eta$ [%]	99.4	99.4	99.5

**Table 6.** Design specification of HS gearbox based on three planetary stages and one parallel stage.

Parameter	First Stage	Second Stage	Third Stage	Fourth Stage
Gear type	Planetary	Planetary	Planetary	Parallel
Gear ratio	1:3.3696	1:3.6923	1:4.7586	1:3.3478
Number of planets	5	3	3	-
Normal module $m$ [mm]	46	30	21	24
Pressure angle $\alpha$ [°]	20	20	20	20
Helix angle $\beta$ [°]	0	0	0	0
Center distance $a$ [mm]	1481	1055	714	1195
Number of teeth, sun/pinion $z_s$ [-]	46	39	29	23
Number of teeth, planet/gear $z_p$ [-]	31	32	38	77
Number of teeth, ring $z_r$ [-]	109	105	109	-
Facewidth sun/pinion $b_s$ [mm]	930	650	420	280
Facewidth planet/gear $b_p$ [mm]	920	630	400	280
Facewidth ring $b_r$ [mm]	960	650	420	-
Profile shift coefficient, sun/pinion $x_s$ [-]	-0.5237	-0.4397	0.2899	0.1391
Profile shift coefficient, planet/gear $x_p$ [-]	0.0266	0.1186	0.2369	-0.3441
Profile shift coefficient, ring $x_r$ [-]	0.8860	0.9998	0.9740	-
Weight gears $m_{gear}$ [ton]	50.5	18.1	6	5.8
Gear mesh efficiency $\eta$ [%]	99.4	99.3	99.5	99.7

**Table 7.** Bearings overview (HS-3P1H).

1st stage	PLC-A	SKF NU 39/1060 ECKMA/HA1
	PLC-B	SKF NU 29/900 ECMA/HB1
	PL-A	SKF NU31/530 ECMA/HB1
	PL-B	SKF NU31/530 ECMA/HB1
2nd stage	PLC-A	SKF NU 20/850 ECMA
	PLC-B	SKF NU 20/600 ECMA
	PL-A	SKF NU 2260 MA
	PL-B	SKF NU 2260 MA
3rd stage	PLC-A	SKF NU 20/600 ECMA
	PLC-B	SKF NU 20/500 ECMA
	PL-A	SKF NU 2344 ECML
	PL-B	SKF NU 2344 ECML
4th stage	IMS-A	SKF NU 2092 ECMA
	IMS-B	SKF NU 2092 ECMA
	HS-A	SKF 32240
	HS-B	SKF 32240

**Table 8.** Bearings overview (MS-3P).

1st stage	PLC-A	SKF NU 39/1060 ECKMA/HA1
	PLC-B	SKF NU 29/900 ECMA/HB1
	PL-A	SKF NU31/530 ECMA/HB1
	PL-B	SKF NU31/530 ECMA/HB1
2nd stage	PLC-A	SKF NU 20/850 ECMA
	PLC-B	SKF NU 20/600 ECMA
	PL-A	SKF NU 2260 MA
	PL-B	SKF NU 2260 MA
3rd stage	PLC-A	SKF NU 20/600 ECMA
	PLC-B	SKF NU 3080 MA
	PL-A	SKF NU 2260 MA
	PL-B	SKF NU 2260 MA

The overall comparison between the different gearboxes for medium- and high-speed drivetrain technologies is given in Table 9. Two different unit costs were assumed, as recommended by KISSsoft, for the cost calculations of the gearbox shafts: one for the sun and pinion shafts (Shafts unit cost<sup>1</sup>) and the other for the rest (Shafts unit cost<sup>2</sup>). As is apparent from Table 9, the high-speed gearbox with three planetary stages and one parallel stage (3P1H) had less weight than the other high-speed gearbox configuration, based on three planetary stages (3P). The weight of HS-3P1H and HS-4P (which was based on four planetary stages) was approximately the same. However, the 4P technology did not help to decrease the weight and, therefore, was not worth the increased complexity of a fourth planetary stage. The high-speed gearbox configuration 3P1H had even less weight than the medium-speed gearbox, even though it had a higher overall gear ratio (considering



the influence of cooling system and housing weight might also influence this conclusion). In [40], the use of four stage gearboxes, based on three planetary stages and one parallel stage and four planetary stages in the medium-speed gearbox, was studied, and it was shown that these gearbox topologies led to an increased weight for the medium-speed gearbox, as also discussed in Section 2.

**Table 9.** Gearbox design results.

<b>Gearbox Specification</b>	<b>MS</b>	<b>HS</b>	<b>HS</b>	<b>HS</b>
Number of stages	3 stages	3 stages	4 stages	
Gear type configuration	3P	3P	3P1H	4P
Number of planets	5,3,3	5,3,3	5,3,3,-	5,3,3,3
Overall gear ratio	1:63.63	1:198.69	1:198.21	1:198.55
Output speed (rpm)	481.1	1502.1	−1498.4	1501
Gear ratio stage 1	1:3.3696	1:3.6842	1:3.3696	1:3.2353
Gear ratio stage 2	1:3.75	1:4.92	1:3.6923	1:3.48
Gear ratio stage 3	1:5.0357	1:10.962	1:4.7586	1:3.6977
Gear ratio stage 4	-	-	1:3.3478	1:4.7692
Weight gears stage 1 (ton)	52.7	61.9	50.5	51
Weight gears stage 2 (ton)	18.9	25.1	18.1	19.5
Weight gears stage 3 (ton)	6.5	23.2	6	4.9
Weight gears stage 4 (ton)	-	-	5.8	1.7
Weight gears (ton)	78	110.2	80.4	77.1
Weight bearings (ton)	12.1	11.6	11.9	11.8
Weight shafts (ton)	84.6	90.1	72.7	76.6
Total weight (ton)	174.7	211.8	165.1	165.4
Gears unit cost (€/kg)	20	20	20	20
Bearings unit cost (€/kg)	100	100	100	100
Shafts unit cost <sup>1</sup> (€/kg)	16	16	16	16
Shafts unit cost <sup>2</sup> (€/kg)	10	10	10	10
Gears cost (M€)	1.56	2.2	1.61	1.54
Bearings cost (M€)	1.21	1.16	1.19	1.18
Shafts cost (M€)	0.85	0.9	0.73	0.77
Total raw material costs (M€)	3.61	4.27	3.53	3.48
Efficiency stage 1	99.4	99.3	99.4	99.4
Efficiency stage 2 (%)	99.4	99.4	99.3	99.5
Efficiency stage 3 (%)	99.5	99.6	99.5	99.6
Efficiency stage 4 (%)	-	-	99.7	99.6
Overall efficiency (%)	98.3	98.3	97.9	98.1
Outer diameter (m)	4.9	4.9	4.75	4.7
Length (m)	4.42	4.56	5.05	5.24

### 3.4. Drivetrain Optimization and Dynamic Analysis Results

#### 3.4.1. Drivetrain Optimization Results

An overview of the three drivetrain configurations under consideration is given in Table 10. The selected results are illustrated in Figure 5. The key performance indices were weight, cost, size, efficiency and electromagnetic torque oscillations. The outer drivetrain diameter was calculated, based on the maximum value between the generator and gearbox outer diameter. The drivetrain length was calculated, based on the summation of gearbox, high-speed shaft and generator length.

**Table 10.** Overall drivetrain systems specifications.

Drivetrain Topology	DD	MS-3P	HS-3P1H
Generator weight (ton)	185.3	57.6	33.1
Gearbox weight (ton)	-	174.7	165.1
Total weight (ton)	185.3	232.3	198.2
Electromagnetic torque oscillation (%)	0.0162	0.0004	0.0005
Efficiency (%)	96.4	97.0	97.1
Length (m)	1.4	5.2	5.9
Outer Diameter (m)	14.2	4.9	4.8

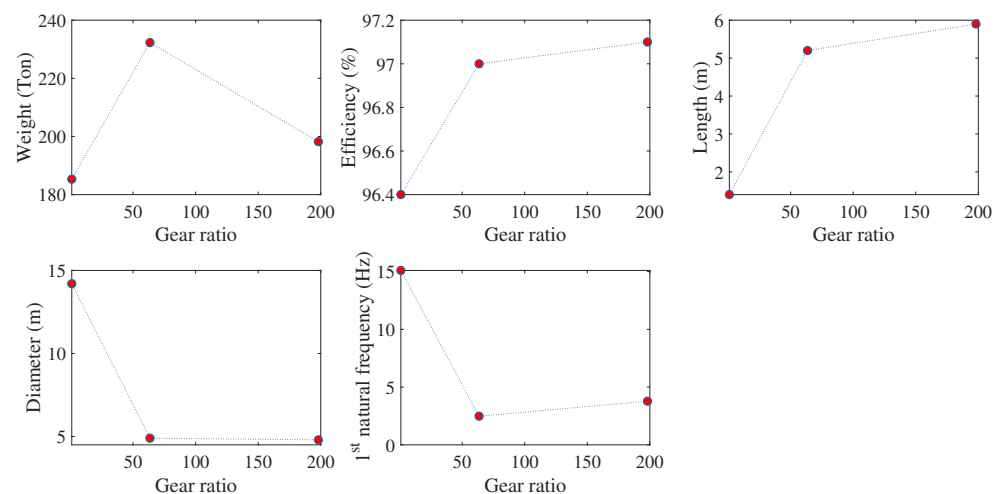


**Figure 5.** Comparison between the three drivetrain technologies under consideration.

As is apparent from Figure 5, the weight comparison of the different drivetrain configurations did not follow the same pattern as reported in [11]. The weight comparison, which was based on a more accurate model of generator and gearbox overall weight, showed that, despite a much heavier generator in direct drive technology, there were still benefits in saving weight by using this generator. It is worth noting that using a different drivetrain layout for direct drive, based on an outer rotor generator, also contributed to the overall weight reduction. Moving from direct drive toward high speed generator, the drivetrain efficiency and length increased while the diameter reduced. For the first torsional natural frequency, the overall utilization of the gearbox seemed to reduce the system natural frequency.

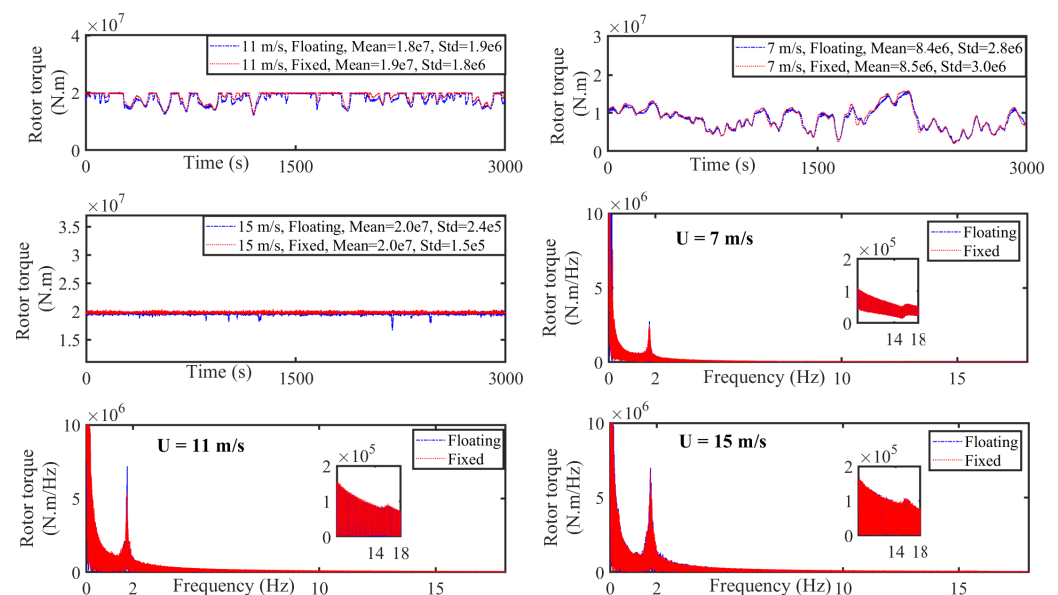
#### 3.4.2. Drivetrain Dynamic Analysis Results

The equivalent dynamic model parameters and natural frequencies of the three drivetrain technologies under consideration are summarized in Table 11. The time domain and the frequency spectrum of the drivetrain low-speed shaft torque for the three different

environmental conditions, representing the turbine operations in below-rated, rated and above rated wind speeds, are shown in Figure 6. The time domain low-speed shaft torque corresponded to one hour of the turbine operation. The first 10 min, which might contain the transients, were removed. The average value and the standard deviation of the torque were specified for the different load cases under consideration in Figure 6. As is apparent from this figure, the standard deviation of the torque, as the indicator of the drivetrain load oscillations and fatigue damage, took the smallest value in the direct-drive technology. The comparison of torque oscillations between the three drivetrain configurations under consideration did not show a significant difference between bottom-fixed and floating turbines in most cases. In rated and above-rated wind speeds, the utilization of the floating platform tended to increase the load oscillations and the fatigue damage of the drivetrain, but in lower than rated wind speeds, the floater helped to compensate for the drivetrain oscillations. This observation was based on only one realization of each load case, and more detailed analysis is required to reach a more accurate conclusion here. Fine tuning of the torque controller to minimize the torque oscillations was not in the scope of this paper.

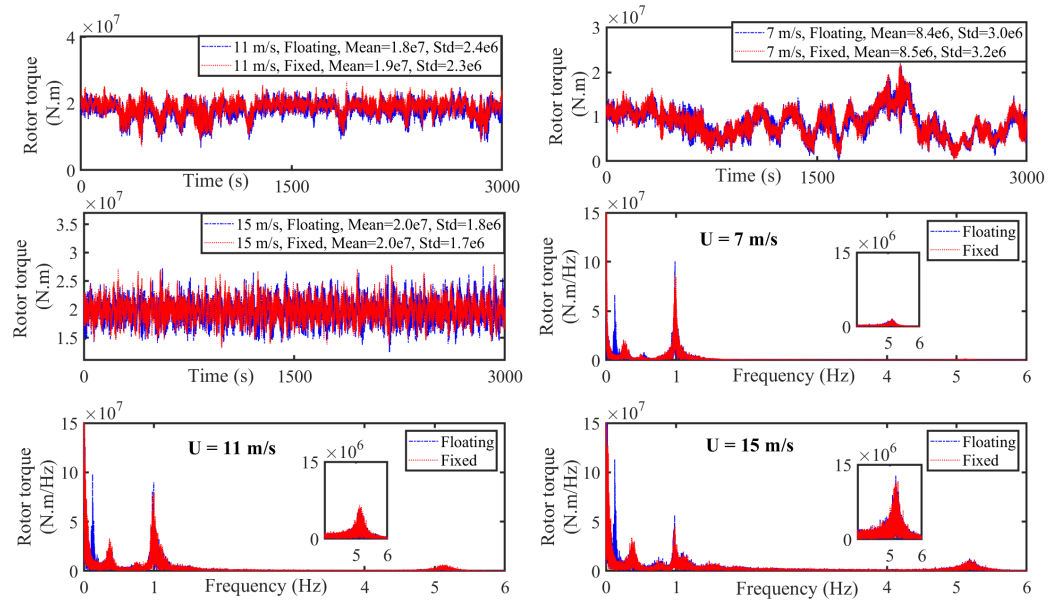
**Table 11.** Drivetrain equivalent dynamic model and natural frequencies.

Drivetrain Technology	DDPMSG	MSPMSG (3P)	HSPMSG (3P1H)
Generator inertia $J_{gen}$ (kg m <sup>2</sup> )	5,772,000	69,018	2698
Rotor inertia $J_r$ (kg m <sup>2</sup> )	350,803,520	350,803,520	350,803,520
Gearbox inertia $J_{gear}$ (kg m <sup>2</sup> )	0	208,803,667	8,628,964
HSS stiffness $k_{gen}$ (Nm/rad)	–	122,523,977	21,556,796
Main shaft stiffness $k_r$ (Nm/rad)	51,140,939,610	51,140,939,610	51,140,939,610
1st natural frequency $f_1^{tor-nonrigid}$ (Hz)	15.10	2.48	3.78
2nd natural frequency $f_2^{tor-nonrigid}$ (Hz)	–	10.42	53.15

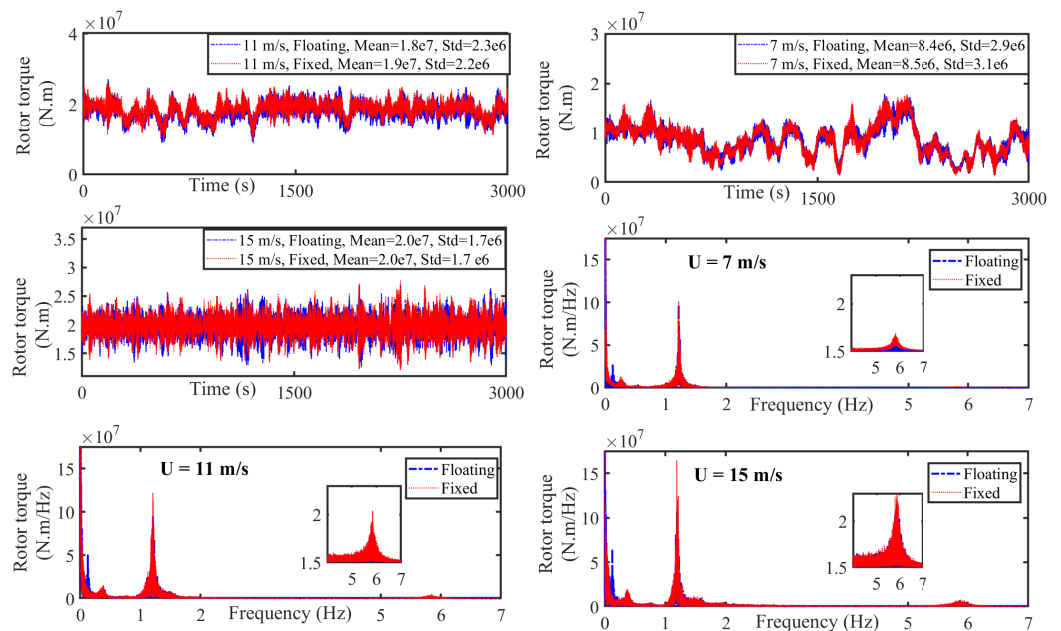


(a) Direct-drive power train configuration.

**Figure 6.** Cont.



(b) Medium-speed power train configuration.



(c) High-speed power train configuration.

**Figure 6.** Rotor torque obtained from turbine-drivetrain coupled simulation in OpenFAST.

Figure 6a shows the turbine simulations with direct-drive power train system. The power train rigid 1.7 Hz and nonrigid 15.6 Hz modes can be seen in all the operating conditions under consideration. The power train torsional natural frequencies are observable in the rotor torque, due to the variation of input wind field, and, therefore, the variation of the rotational speed of the rotor shaft which acted as impulse to the system [56].

Figure 6b shows the turbine simulations with a medium-speed power train system. The power train rigid 1.0 Hz and nonrigid 5.1 Hz modes can be seen in all the operating conditions in both bottom-fixed and floating simulations.

Figure 6c shows the turbine simulations with a high-speed power train system. The power train rigid 1.2 Hz and nonrigid 5.8 Hz modes can be seen in all the operating conditions in both bottom-fixed and floating simulations. The main rotational frequency

0.12 Hz and its 3P (blade passing frequency) and 6P harmonics are also shown in both medium- and high-speed drivetrain simulations.

From the dynamics point of view, the direct-drive power train's first rigid and nonrigid modes took place in a safer distance from the rotor rotational frequency and its harmonics, the expected ocean wave frequencies 0.04–0.48 Hz, the first and second tower modes, and also blades and tower-substructure modes. However, the generator electromagnetic torque oscillations in the direct-drive technology happened at a lower frequency and had a higher amplitude of oscillations, compared to the medium- and high-speed generators, which was a negative point.

The dynamic analyses results also indicated a difference between the first drivetrain nonrigid mode calculated from the drivetrain decoupled model, as reported in Table 11, and the drivetrain nonrigid mode from the turbine-drivetrain coupled analysis in OpenFAST (2.5 Hz compared to 5.1 Hz in medium-speed, and 3.8 Hz compared to 5.8 Hz in high-speed). The latter showed that the drivetrain decoupled dynamic behavior could be different from the actual turbine-power train coupled dynamics, which might limit the domain of applicability of the drivetrain decoupled analysis approach.

#### 4. Concluding Remarks

The coupled generator–gearbox design of the most common drivetrain technologies for 15 MW offshore wind turbines was presented. These configurations were all based on PMSG with or without a gearbox to realize direct-drive, medium- and high-speed drivetrain technologies. The design procedure started from optimal analytical design at the component-level supported by design validation in secondary software, which also provided the more detailed specification of the designed components. This detailed specification provided the basis for the comparison study between the different configurations to see how the utilization of a gearbox with the different gear ratios influenced the overall weight, efficiency, length, diameter, natural frequencies and the torque oscillations of the drivetrain. This study showed that the utilization of the direct-drive configuration for 15 MW wind turbine application could:

- help to reduce the overall weight and length of the drivetrain,
- cause increase in the overall diameter and the generator electromagnetic torque oscillations and reduction of overall efficiency.

The drivetrain-turbine coupled dynamic analysis was performed, using the simplified models of the designed drivetrain systems, where the drivetrain–turbine coupled natural frequencies and the possibility of resonance with the external excitation frequencies were investigated. The dynamic analysis results showed that:

- in all the three designed drivetrain technologies, the drivetrain natural frequencies took a distance from the external excitation and structural frequencies, though the direct-drive generator took a safer distance over the turbine power production range,
- in the direct-drive, compared to the other two configurations, the oscillations of the torque applied to the input shaft of drivetrain reduced, which implied more robustness and potentially less fatigue damage of direct-drive when confronting with environmentally- and structurally-induced loads.

There was uncertainty in the inputs applied to this research, such as the unit prices of the materials used for the components costs calculations, which could influence the conclusions made in this paper. Exposing the coupled model, based on the designed drivetrain systems to all the load cases, and performing detailed reliability analysis, is considered to be future work.

**Author Contributions:** Conceptualization, F.K.M.; Methodology, F.K.M.; Software, F.K.M. and N.D.; Validation, F.K.M. and N.D.; Formal Analysis, F.K.M. and N.D.; Writing—Original Draft Preparation, F.K.M.; Writing—Review & Editing, F.K.M. and N.D. All authors have read and agreed to the published version of the manuscript.



**Funding:** This research received no external funding.

**Data Availability Statement:** The code enabling the replication of the gearbox design can be found at <https://github.com/faridkm/Wind-turbine-gearbox-optimization>, accessed on 15 November 2021.

**Acknowledgments:** The authors would like to thank Jonathan Keller from the National Renewable Energy Laboratory, Pablo Carazo Morales from Iberdrola, and Ashkan Rezaei from the Norwegian University of Science and Technology for sharing their insights, which helped to improve the quality of presentations of this paper.

**Conflicts of Interest:** The authors declare no conflict of interest.

## References

1. Moghadam, F.; Chabaud, V.; Gao, Z.; Chapaloglou, S. Power Train Degradation Modelling for Multi-objective Active Power Control of Wind Farms. *Eng. Res.-Forsch. Ingenieurwesen* **2022**, *accepted*.
2. Shaw, W.J.; Berg, L.K.; Debnath, M.; Deskos, G.; Draxl, C.; Ghate, V.P.; Hasager, C.B.; Kotamarthi, R.; Mirocha, J.D.; Muradyan, P.; et al. Scientific challenges to characterizing the wind resource in the marine atmospheric boundary layer. *Wind. Energy Sci.* **2022**, *7*, 2307–2334. [[CrossRef](#)]
3. Shields, M.; Beiter, P.; Nunemaker, J.; Cooperman, A.; Duffy, P. Impacts of turbine and plant upsizing on the levelized cost of energy for offshore wind. *Appl. Energy* **2021**, *298*, 117189. [[CrossRef](#)]
4. Durakovic, A. World's First 16 MW Offshore Wind Turbine Rolls off Production Line. Available online: <https://www.offshorewind.biz/2022/11/24/worlds-first-16-mw-offshore-wind-turbine-rolls-off-production-line/> (accessed on 24 November 2022).
5. Ashuri, T.; Martins, J.R.; Zaaijer, M.B.; van Kuik, G.A.; van Bussel, G.J. Aeroservoelastic design definition of a 20 MW common research wind turbine model. *Wind Energy* **2016**, *19*, 2071–2087. [[CrossRef](#)]
6. Yao, S.; Chetan, M.; Griffith, D.T.; Escalera Mendoza, A.S.; Selig, M.S.; Martin, D.; Kianbakht, S.; Johnson, K.; Loth, E. Aerostructural design and optimization of 50 MW wind turbine with over 250-m blades. *Wind Eng.* **2022**, *46*, 273–295. [[CrossRef](#)]
7. Abdelmoteleb, S.E.; Mendoza, A.S.E.; dos Santos, C.R.; Bachynski-Polić, E.E.; Griffith, D.T.; Oggiano, L. Preliminary Sizing and Optimization of Semisubmersible Substructures for Future Generation Offshore Wind Turbines. *J. Phys. Conf. Ser.* **2022**, *2362*, 012001. [[CrossRef](#)]
8. Stehly, T.; Duffy, P. *2020 Cost of Wind Energy Review*; Technical Report; National Renewable Energy Lab. (NREL): Golden, CO, USA, 2021.
9. Chen, W.; Wang, X.; Zhang, F.; Liu, H.; Lin, Y. Review of the application of hydraulic technology in wind turbine. *Wind Energy* **2020**, *23*, 1495–1522. [[CrossRef](#)]
10. Moghadam, F.K.; Nejad, A.R. Online condition monitoring of floating wind turbines drivetrain by means of digital twin. *Mech. Syst. Signal Process.* **2022**, *162*, 108087. [[CrossRef](#)]
11. Moghadam, F.K.; Nejad, A.R. Evaluation of PMSG-based drivetrain technologies for 10-MW floating offshore wind turbines: Pros and cons in a life cycle perspective. *Wind Energy* **2020**, *23*, 1542–1563. [[CrossRef](#)]
12. Sethuraman, L.; Maness, M.; Dykes, K. Optimized generator designs for the DTU 10-MW offshore wind turbine using GeneratorSE. In Proceedings of the 35th Wind Energy Symposium, Grapevine, TX, USA, 9–13 January 2017; p. 0922.
13. Carroll, J.; McDonald, A.; McMillan, D. Reliability comparison of wind turbines with DFIG and PMG drive trains. *IEEE Trans. Energy Convers.* **2014**, *30*, 663–670. [[CrossRef](#)]
14. Murthy, K.V. *Computer-Aided Design of Electrical Machines*; BS Publications Hyderabad: Hyderabad, India, 2008.
15. Li, H.; Chen, Z.; Polinder, H. Optimization of multibrid permanent-magnet wind generator systems. *IEEE Trans. Energy Convers.* **2009**, *24*, 82–92. [[CrossRef](#)]
16. Harzendorf, F.; Schelenz, R.; Jacobs, G. Reducing cost uncertainty in the drivetrain design decision with a focus on the operational phase. *Wind Energy Sci.* **2021**, *6*, 571–584. [[CrossRef](#)]
17. Harzendorf, F.; Schelenz, R.; Jacobs, G. Method for holistic wind turbine drivetrain comparison exemplarily applied to geared and direct drive systems. *Forsch. Ingenieurwesen* **2022**, *86*, 21–33. [[CrossRef](#)]
18. Jenkins, B.; Carroll, J.; McMillan, D. O&M cost modelling of major replacements in next-generation offshore wind turbines. In Proceedings of the 11th Renewable Power Generation Conference—RPG, London, UK, 22–23 September 2022; pp. 2227–2234.
19. GE. AN INDUSTRY FIRST Haliade-X Offshore Wind Turbine. Available online: <https://www.ge.com/renewableenergy/wind-energy/offshore-wind/haliade-x-offshore-turbine> (accessed on 20 January 2023).
20. SSE. Turbine Supply Contract for Seagreen Finalised. 2020. Available online: <https://www.sse.com/news-and-views/2020/06/turbine-supply-contract-for-seagreen-finalised> (accessed on 23 January 2023).
21. SKF. Bearing Arrangements for Wind Turbine Main Shafts. Available online: <https://www.skf.com/id/industries/wind-energy/drivetrain/main-shaft/bearing-arrangements> (accessed on 23 January 2023).
22. Schmid, P. How Large Offshore Wind Turbines Are Challenging Bearing Designs. Available online: <https://www.windpowerengineering.com/large-offshore-wind-turbines-challenging-bearing-designs> (accessed on 23 February 2018).

23. OpenPR. Direct Drive Wind Turbine Market Growth Analysis by Top Leading Players-Goldwind, Enercon, Siemens, GE Energy, EWT, Lagerwey Wind, Leitwind, United Energies MTOI. Available online: <https://www.openpr.com/news/1240894/direct-drive-wind-turbine-market-growth-analysis-by-top-leading-players-goldwind-enercon-siemens-ge-energy-ewt-lagerwey-wind-leitwind-united-energies-mtoi.html> (accessed on 17 September 2018).
24. Gamesa, S. Siemens Gamesa Renewable Energy Is Ready for the Future. Available online: <https://www.bila-automation.com/case-stories/wind/siemens-gamesa-renewable-energy> (accessed on 23 January 2023).
25. POWER, Z.W. Harnessing the Power of the Wind with Simcenter Solutions. Available online: <https://www.plm.automation.siemens.com/global/de/our-story/customers/zf-wind-power/67899> (accessed on 23 January 2023).
26. ABB. PCS6000 Medium Voltage Wind Turbine Converter. Available online: <https://new.abb.com/power-converters-inverters/wind-turbines/utility-scale/pcs6000> (accessed on 23 January 2023).
27. Zhu, R.; Peng, W.; Wang, D.; Huang, C.G. Bayesian transfer learning with active querying for intelligent cross-machine fault prognosis under limited data. *Mech. Syst. Signal Process.* **2023**, *183*, 109628. [CrossRef]
28. Hart, E.; Clarke, B.; Nicholas, G.; Kazemi Amiri, A.; Stirling, J.; Carroll, J.; Dwyer-Joyce, R.; McDonald, A.; Long, H. A review of wind turbine main bearings: design, operation, modelling, damage mechanisms and fault detection. *Wind Energy Sci.* **2020**, *5*, 105–124. [CrossRef]
29. Lagerström, A. Design of Large pm-Generators for Wind Power Applications. Master's Thesis, NTNU, Trondheim, Norway, 2011.
30. Structural analysis and optimisation of transverse flux permanent magnet machines for 5 and 10 MW direct drive wind turbines. *Wind Energy* **2012**, *15*, 19–43. [CrossRef]
31. Zavvos, A.; McDonald, A.; Mueller, M. Structural optimisation tools for iron cored permanent magnet generators for large direct drive wind turbines. In Proceedings of the IET Conference on Renewable Power Generation (RPG 2011), Edinburgh, UK, 6–8 September 2011; pp. 1–6. [CrossRef]
32. Taras, P.; Nilifard, R.; Zhu, Z.Q.; Azar, Z. Cooling techniques in direct-drive generators for wind power application. *Energies* **2022**, *15*, 5986. [CrossRef]
33. Gieras, J.F. Analytical approach to cogging torque calculation of PM brushless motors. *IEEE Trans. Ind. Appl.* **2004**, *40*, 1310–1316. [CrossRef]
34. Zhu, L.; Jiang, S.; Zhu, Z.; Chan, C. Comparison of alternate analytical models for predicting cogging torque in surface-mounted permanent magnet machines. In Proceedings of the 2008 IEEE Vehicle Power and Propulsion Conference, Harbin, China, 3–5 September, 2008; pp. 1–6.
35. Gieras, J.F. *Permanent Magnet Motor Technology: Design and Applications*; CRC Press: Boca Raton, FL, USA, 2009.
36. Burton, T.; Jenkins, N.; Sharpe, D.; Bossanyi, E. *Wind Energy Handbook*; John Wiley & Sons: Hoboken, NJ, USA, 2011.
37. Anaya-Lara, O.; Tande, J.O.; Uhlen, K.; Merz, K. *Offshore Wind Energy Technology*; Wiley: Hoboken, NJ, USA; Chichester, UK, 2018.
38. Wang, S.; Nejad, A.R.; Moan, T. On design, modelling, and analysis of a 10-MW medium-speed drivetrain for offshore wind turbines. *Wind Energy* **2020**, *23*, 1099–1117. [CrossRef]
39. de Vries, E. Exclusive: How Vestas Beat Rivals to Launch First 15 MW Offshore Turbine. Available online: [https://www.windpowermonthly.com/article/1706924/exclusive-vestas-beat-rivals-launch-first-15mw-offshore-turbine?utm\\_medium=EMAIL](https://www.windpowermonthly.com/article/1706924/exclusive-vestas-beat-rivals-launch-first-15mw-offshore-turbine?utm_medium=EMAIL) (accessed on 10 February 2021).
40. Desch, N. Drivetrain Design for IEA Wind 15 MW Offshore Reference Wind Turbine under Consideration of Sensor Integration for Condition Monitoring. Unpublished Master's Thesis, Norwegian University of Science and Technology in Norway, Trondheim, Norway; Technical University Darmstadt in Germany, Darmstadt, Germany, 2022.
41. Klocke, F.; Brecher, C. *Zahnrad- und Getriebetechnik: Auslegung–Herstellung–Untersuchung–Simulation*; Carl Hanser Verlag GmbH Co KG: München, Germany, 2016.
42. Linke, H. (Ed.) *Stirnräderverzahnung: Berechnung–Werkstoffe–Fertigung*; 2., Vollst. überarb. Aufl. ed.; Hanser: München, Germany; Wien, Austria, 2010.
43. International Standard. IEC 61400-4 Wind Turbines: Part 4: Design Requirements for Wind Turbine Gearboxes. Available online: <https://www.iso.org/standard/44298.html> (accessed on 23 January 2023).
44. Guo, Y.; Parsons, T.; King, R.; Dykes, K.; Veers, P. *Analytical Formulation for Sizing and Estimating the Dimensions and Weight of Wind Turbine Hub and Drivetrain Components*; National Renewable Energy Lab. (NREL): Golden, CO, USA, 2015. [CrossRef]
45. Moghadam, F.K. Wind-Turbine-Gearbox-Optimization. Available online: <https://github.com/faridkm/Wind-turbine-gearbox-optimization> (accessed on 15 November 2021).
46. Moghadam, F.K.; Rebouças, G.F.d.S.; Nejad, A.R. Digital twin modeling for predictive maintenance of gearboxes in floating offshore wind turbine drivetrains. *Forsch. Ingenieurwesen* **2021**, *85*, 273–286. [CrossRef]
47. NREL. OpenFAST Documentation. v3.2.0. Available online: <https://ap-openfast.readthedocs.io/en/mdv2-farm/source/user/index.html#> (accessed on 9 September 2022).
48. IEC 61400-1:2019; Wind Energy Generation Systems, Part 1: Design Requirements. International Electrotechnical Commission: Geneva, Switzerland, 2019.
49. Gaertner, E.; Rinker, J.; Sethuraman, L.; Zahle, F.; Anderson, B.; Barter, G.E.; Abbas, N.J.; Meng, F.; Bortolotti, P.; Skrzypinski, W.; et al. *IEA Wind TCP Task 37: Definition of the IEA 15-Megawatt Offshore Reference Wind Turbine*; Technical Report; National Renewable Energy Lab. (NREL): Golden, CO, USA, 2020.

50. Allen, C.; Viscelli, A.; Dagher, H.; Goupee, A.; Gaertner, E.; Abbas, N.; Hall, M.; Barter, G. *Definition of the UMaine VoltturnUS-S Reference Platform Developed for the IEA Wind 15-Megawatt Offshore Reference Wind Turbine*; Technical Report; National Renewable Energy Lab. (NREL): Golden, CO USA; Univ. of Maine: Orono, ME, USA, 2020.
51. Johannessen, K.; Meling, T.S.; Hayer, S. Joint distribution for wind and waves in the northern north sea. In Proceedings of the Eleventh International Offshore and Polar Engineering Conference, Stavanger, Norway, 17–22 June 2001.
52. Copper. Available online: <https://www.dailymetalprice.com/metalpricescurr.php?x=USD> (accessed on 23 January 2023).
53. Laminated Iron. Available online: [https://www.google.com/search?q=laminated+iron+price&rlz=1C1GCEA\\_enNO995NO995&oq=laminated+iron+price&aqs=chrome..69i57j0i15i22i30.4808j0j7&sourceid=chrome&ie=UTF-8](https://www.google.com/search?q=laminated+iron+price&rlz=1C1GCEA_enNO995NO995&oq=laminated+iron+price&aqs=chrome..69i57j0i15i22i30.4808j0j7&sourceid=chrome&ie=UTF-8) (accessed on 23 January 2023).
54. Cast Iron. Available online: <https://www.yidecasting.com/cast-iron-price> (accessed on 23 January 2023).
55. Rare Earth Element Prices. Available online: <https://strategicmetalsinvest.com/current-strategic-metals-prices/> (accessed on 23 January 2023).
56. Moghadam, F.K.; Nejad, A.R. Theoretical and experimental study of wind turbine drivetrain fault diagnosis by using torsional vibrations and modal estimation. *J. Sound Vib.* **2021**, *509*, 116223. [[CrossRef](#)]

**Disclaimer/Publisher’s Note:** The statements, opinions and data contained in all publications are solely those of the individual author(s) and contributor(s) and not of MDPI and/or the editor(s). MDPI and/or the editor(s) disclaim responsibility for any injury to people or property resulting from any ideas, methods, instructions or products referred to in the content.